Modelling, Measurement and Control B
Vol. 87, No. 3, September, 2018, pp. 129-134
Journal homepage: http://iieta.org/Journals/MMC/MMC_B

Synthesis and characterization of Fe_2o_3/reduced graphene oxide nanocomposite as a high-performance anode material for sodium-ion batteries

Vincenza Modafferi[1], Michele Fiore[2], Enza Fazio[3], Salvatore Patanè[3], Claudia Triolo[3], Saveria Santangelo[1], Riccardo Ruffo[2], Fortunato Neri[3], Maria G. Musolino[1*]

[1] DICEAM, Università Mediterranea di Reggio Calabria, Reggio Calabria 89122, Italy
[2] Dipartimento di Scienza dei Materiali, Università di Milano Bicocca, Milano 20125, Italy
[3] MIFT, Università di Messina, Messina 98166, Italy

Corresponding Author Email: mariagrazia.musolino@unirc.it

https://doi.org/10.18280/mmc_b.870303

Received: 5 March 2018
Accepted: 16 April 2018

Keywords:
α - Fe_2O_3, reduced graphene oxide, solvothermal method, anode, sodium-ion batteries

ABSTRACT

Hematite/reduced graphene oxide (Fe_2O_3/rGO) nanocomposite was successfully fabricated via a facile solvothermal reaction of iron precursor solution and GO leading to simultaneous deposition of iron oxide nanoparticles and *in situ* reduction of GO without any reducing agent. Texture and morphology, microstructure, chemical and surface composition of the nanocomposite were investigated by scanning electron microscopy, X-ray diffraction, Raman spectroscopy, thermo-gravimetric analysis and X-ray photoelectron spectroscopy, respectively. Its electrochemical performance as anode material for sodium ion batteries was preliminarily evaluated via galvanostatic cycling. The results prove that the Fe_2O_3 nanoparticles are uniformly anchored onto the surface of graphene nanosheets and that the Fe_2O_3/rGO nanocomposite shows interestingly higher specific capacities compared to the bare Fe_2O_3.

1. INTRODUCTION

Electrochemical energy storage (EES) is a very important issue owing to the rapid growth of markets for portable electronic devices, electric/hybrid vehicles, grid-scale energy storage systems [1-2]. Rechargeable lithium-ion batteries (LIBs) currently represent the most promising EES systems, due to relative high energy density and long-term cycle life [3-4].

However, the scarcity of lithium resources in the Planet limits their large-scale implementation, especially in the automotive field. Thanks to the greater abundance, lower cost and similar chemistry of sodium, sodium-ion batteries (SIBs) are emerging as a more sustainable alternative to LIBs [5-7].

Unfortunately, the larger ionic radius of sodium (0.102 nm) as compared to that of the lithium (0.076 nm) leads to the sluggish Na^+ ions diffusion kinetics into the host materials, because larger channels for transport and interstitial sites for sodium ions are required [8].

Therefore, the design of highly performing, sustainable and environmentally friendly electrode materials is the key factor for accelerating the commercialization of SIBs.

Different from cathode materials, anode materials still represent a challenge for the development of SIB technology. The production of hard carbons, regarded as promising anode materials, has great environmental impact [9].

Transition metal oxides (TMOs) are gathering attention as alternative anode materials for SIBs. Among them, hematite (α-Fe_2O_3) is particularly appealing because of its low-toxicity, environmental friendliness and high theoretical capacity (1007 mAh/g) [10-11].

Graphene, generally obtained by chemical reduction of graphene oxide (GO), is used as a conducting additive for hybrid nanostructured materials because of its large specific surface area, excellent electrical conductivity, chemical inertness, and rapid heterogeneous electron transfer [12].

Recently, graphene/TMO-based nanocomposites have attracted great interest as electrodes due to the positive synergistic effects between graphene and TMOs. It is well accepted that compared to bare metal oxides, the hybrid systems possess better electrochemical performance and limit detrimental effects of the volume expansion/contraction during charge/discharge process [13-14].

This work deals with the simple synthesis of hematite/ reduced graphene oxide (Fe_2O_3/rGO) nanocomposite, its characterization by means of a combination of complementary techniques, and its electrochemical testing as anode material in SIBs.

2. EXPERIMENTAL SECTION

2.1 Synthesis of Fe_2O_3/rGO nanocomposite

Graphene oxide was prepared by exfoliation of graphite powder following a slightly modified Hummers method [15]. In a typical synthesis 2 g of graphite and 1 g of $NaNO_3$ were mixed with 50 ml of concentrated H_2SO_4 and stirred in an ice bath. Subsequently, $KMnO_4$ (7 g) was slowly added into the mixture under stirring and cooling. The mixture was stirred for 2h at 35 °C. The temperature was then increased to about 98 °C and distilled water (400 ml) was added followed by a slow addition of 10 ml of H_2O_2 under stirring. The as-obtained GO was then recovered through centrifugation and thoroughly washed with HCl aqueous solution and with distilled water, in sequence. Finally, the solid was dried at 50 °C in a vacuum

oven for 2 days.

The nanocomposite was obtained by simple solvothermal treatment. 200 mg of GO were dispersed in 60 ml of ethanol through sonication for 2 h. Then, 10 ml of a 0.2 M solution of Fe $(CH_3COO)_2$ were added. The reaction mixture was stirred at 80 °C for 10 h and, subsequently, was transferred in a stainless steel autoclave for solvothermal treatment at 170 °C for 3 h. The resulting product was centrifuged, washed with ethanol and distilled water for several times and then dried in air. For comparison, Fe_2O_3 nanoparticles and rGO were also synthesized by the similar procedure except for the absence of graphene oxide and Fe $(CH_3COO)_2$, respectively.

2.2 Material characterization

The sample texture and morphology were investigated by scanning electron microscopy (SEM). Analysis was performed using a Phenom Pro-X scanning electron microscope equipped with an energy-dispersive X-ray (EDX) spectrometer.

The formation of GO and its subsequent reduction to rGO upon thermal treatment were ascertained by means of X-ray powder diffraction (XRD). The crystalline phase of the oxide was identified by XRD and micro-Raman spectroscopy (MRS). The XRD patterns were recorded at RT by using the Ni β-filtered Cu-Ka radiation (λ = 0.15404 nm) at 40 KV. Analyses were registered in the 2θ range of 10° – 80° at a scan speed of 0.5° min^{-1}. Diffraction-peak identification was performed on the basis of the JCPDS database of reference compounds. Raman scattering excited by an Ar-ion laser operating at 532 nm (2.33 eV) was measured in air at RT with NTEGRA - Spectra SPM from NT-MDT spectrometer equipped with a confocal microscope by using a 100X objective. The use of a very low laser power (250 μW at the sample surface) prevented local heating of the samples and annealing effects.

The chemical composition of the resulting composite was determined by thermo-gravimetric analysis (TGA) in a NETZSCH STA 449C instrument. The sample was heated from 25 to 1000 °C in air, and the heating rate was 10 °C/min. Surface composition of the samples and chemical environment of the component species were investigated by X-ray photoelectron spectroscopy (XPS). Spectra were acquired using a K-Alpha system of Thermo Scientific, equipped with a monochromatic Al-Kα source (1486.6 eV) and operating in constant analyser energy mode with a pass energy of 50 eV for high resolution spectra and a spot size of 400 μm. The elemental concentrations were estimated from the areas under the photoelectron peaks weighed by the relative sensitivity factors. Identification and quantification of the surface species were carried out by decomposing the high-resolution photoelectron spectra of core levels. The binding energy shifts were calibrated keeping the C 1*s* position fixed at 284.5 eV.

2.3 Electrochemical testing measurements

Galvanostatic cycling with potential limitation (GCPL) was carried out using the BioLogic VSP-300 multichannel potentiostat-galvanostat. Two-electrode coin cells CR2032 assembled in an argon filled glove box (MBraun), with sodium acting both as counter and reference electrode, were cycled at C/20 (50 mA/g) between 0.01 V and 3.00 V vs Na/Na^+.

The electrode of the bare rGO was cycled at the same current density of the rGO in the nanocomposite. The working electrodes with the Fe_2O_3/rGO composite were prepared mixing the as prepared active material, the carbon matrix (Super P, MM Carbon) and the polymer binder (Polyacrylic Acid Mw ~450000, Sigma Aldrich) in the weight ratio 8:1:1, respectively. Instead, higher carbon content has been used in the electrode with the hematite alone to equal the total amount of carbon of the composite electrode.

The carbon used in the preparation of the electrode was pretreated at 800°C in argon atmosphere to remove the adsorbed water and impurities, reducing the typical irreversibility that occurs during the first charge and discharge in such systems [16]. The slurry obtained suspending the solid in N-Methyl-2-pyrrolidone (ACS Reagent, 99%) solvent, was casted onto a copper foil using doctor blade technique and dried until complete evaporation of the solvent at 80°C under vacuum overnight. The working electrode was finally roll pressed and 16 mm diameter disks were punched out. The load of active material was ~1 mg/cm^2.

3. RESULTS AND DISCUSSION

Figure 1 shows the morphology of the samples, as resulting from the SEM analysis. All the samples exhibit a porous structure. No agglomeration of Fe_2O_3 nanostructures is observed on the Fe_2O_3/rGO hybrid (Figure 1d), suggesting that graphene nanosheets are coated with Fe_2O_3 nanostructures. The formation of GO from graphite is ascertained by means of XRD. The XRD pattern of the sample (curve a in Fig. 2) shows the sharp and characteristic diffraction peak at 2θ = 9.5°, corresponding to the (001) reflection of graphene oxide with d-spacing of 0.955 nm. Its 2θ-angle position, matching well with the values reported in the literature [17], suggests that GO sheets are loosely stacked due to the presence of oxygen-containing functional groups (C=O, –COOH, –OH, C–O–C) between the layer of graphite formed during oxidation. The minor reflection at 42.6° suggests a turbostratic disorder in graphene sheets [18]. After the solvothermal treatment (curve b in Fig. 2) the characteristic peak of GO disappears, confirming the occurrence of the thermal reduction to rGO. A very broad and intense peak around 2 = 24.1° and a weaker one around at 2 = 43.2° are detected. The latter can be ascribed to the reflection from (100) planes of rGO. The former corresponds to the reflection from (002) planes with a *d*-spacing value of 0.369 nm. The remarkable decrease of interlayer spacing confirms the removal of most of the oxygen-containing functional groups [19].

The same considerations apply to the nanocomposite sample (curve c in Fig. 2). No typical diffraction peak of GO is observed in its XRD pattern, proving the successful reduction of GO to rGO during the solvothermal treatment also in the presence of the iron oxide precursor. The similarity between patterns relative to bare oxide and nanocomposite (curves d and c in Fig. 2, respectively) indicate that the same crystalline phase of the oxide is formed in the two cases. The diffraction peaks at 2 = 24.1°, 33.2°, 35.8°, 40.9°, 49.5°, 53.9°, 57, 5°, 62.6° and 64.1° can be indexed to the (0 1 2), (1 0 4), (1 1 0), (1 1 3), (0 2 4), (1 1 6), (122), (2 1 4) and (3 0 0) crystal planes of the rhombohedral (hexagonal) structure of hematite (JCPDS card no. 33-0664), respectively [20]. No other peaks are observed suggesting high phase-purity of the as-synthesized samples. The average size of -Fe_2O_3 crystallites, evaluated from the main (104) peak of the diffractogram by using the Scherrer equation, is 24.1 nm for

bare Fe_2O_3 and 27.2 nm for Fe_2O_3/rGO nanocomposite. It is worth noting that none of typical peaks belonging to rGO are observed in the XRD spectrum of Fe_2O_3/rGO. This is probably due to the low diffraction intensity of rGO.

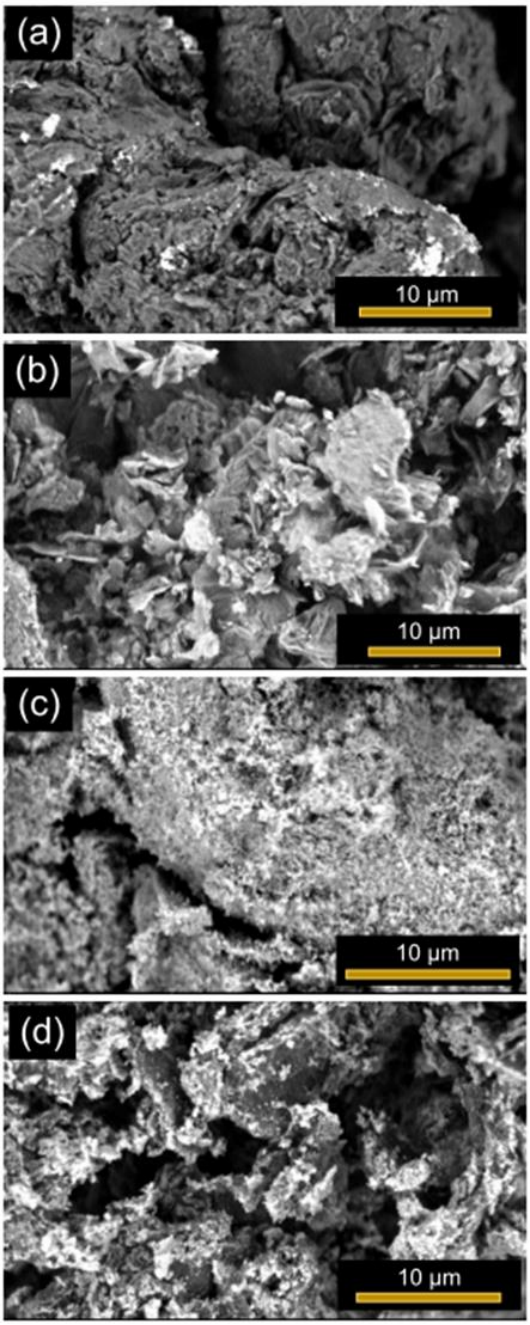

Figure 1. SEM images: (a) GO, (b) rGO, (c) bare Fe2O3 and (d) Fe2O3/rGO nanocomposite

The content of graphene nanosheets in Fe_2O_3/rGO nanocomposite is estimated by TGA in air flow (Figure 3). The weight loss between 350 and 620 °C is ascribed to the combustion of rGO and is calculated to be about 48 wt%.

The Raman fingerprint of rGO [17] is fairly visible in the spectrum of the Fe_2O_3/rGO nanocomposite (Figure 4), as evident from the comparison with the spectrum of rGO. The Raman profile peculiar to highly disordered graphitic carbons consists of two intense and broad features located at ~1360 cm^{-1} and ~1590 cm^{-1} dominating the spectra. The former (D-band) is generated by finite size effects and by lattice defects breaking the translational symmetry of graphitic layers [21]. The latter (G-band) originates from the stretching of C=C pairs and is the fingerprint of the graphitic crystalline arrangement. In the higher frequency region of the spectrum, overtones and combination bands are detected. The D/G integrated intensity ratio (I_D/I_G) is commonly utilized to monitor the sp^2 defect density in the carbon lattice [22]. The frequency position of the G-band band (ω_G) monitors the local strength of carbon bonds [22-23] and is sensitive to charge transfer, local distortions and hybridization changes of the C–C bonding. In oxygen-functionalized carbons, the bands upshift as an effect of the electron transfer from the π-states to the oxygen atoms.

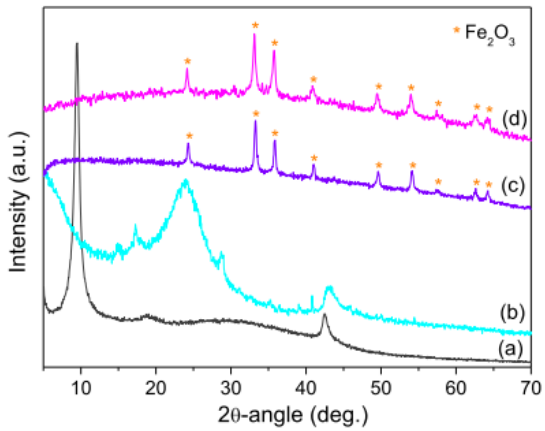

Figure 2. XRD patterns of (a) GO, (b) rGO, (c) Fe2O3/rGO nanocomposite, (d) bare Fe2O3 nanoparticles

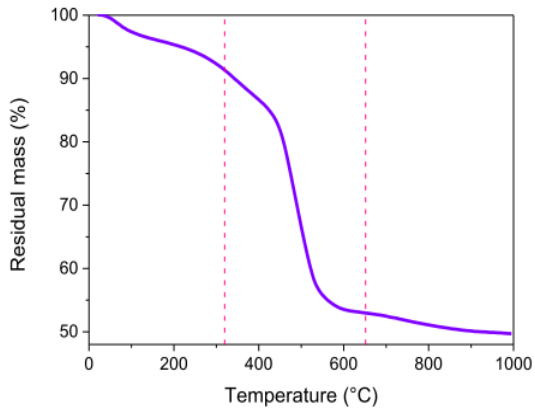

Figure 3. TGA profile of Fe_2O_3/rGO nanocomposite

As for rGO, the comparison with GO (Figure. 4) proves that the oxidation degree diminishes as an effect of the solvothermal treatment, and the π network is partly restored. In fact, the G-band shifts (from 1600 cm^{-1} in GO) down to 1588 cm^{-1}, and the D band slightly intensifies relative to the G-band (I_D/I_G increases from 2.75 in GO to 3.01 in rGO). The decrease of ω_G is the effect of the smaller oxidation degree of the sample [23-24], whereas the enhancement of the I_D/I_G ratio indicates that the density of sp^2 carbon defects (which solely contribute to the D-band intensity) increases at expenses of non-sp^2 defects, with consequent non-sp^2/sp^2 defect density lowering with respect to GO.

Having a rhombohedral unit cell formed by chains of Fe_2O_9 dimers, α-Fe_2O_3 belongs to the crystal space group D^3_{d6}. Normal modes predicted by the factor group analysis include six IR-active vibrations ($2A_{2u} + 4E_u$) and seven Raman-active vibrations ($2A_{1g} + 5E_g$) [24,25]. Actually six peaks, at 224, 244,

293, 407, 496 and 609 cm^{-1}, are detected in the lower frequency region of the Raman spectrum (Figure 4) corresponding to the $A_{1g}(1)$, $E_g(1)$, unresolved $E_g(2)$-$E_g(3)$, $E_g(4)$, $A1_g(2)$ and $E_g(5)$ vibration modes of α-Fe_2O_3, respectively. In addition, a very intense asymmetric feature peaking at ~1315 cm^{-1} and a very weak peak at ~660 cm^{-1} are detected. The latter feature, typical of nanocrystalline hematite, originates from the presence of surface defects and/or reduced grain size which, relaxing selection rules, render Raman active the IR-active E_u mode [26,27]. The former band is ascribed to two-phonon scattering or two-magnon scattering [27-28]. In rGO/Fe_2O_3 this band partly overlaps to the D-band arising from rGO.

Figure 5 displays high-resolution photoelectron spectra (HRXPS) of the C 1*s*, O 1*s*, and Fe 2*p* core levels in the Fe_2O_3/rGO nanocomposite.

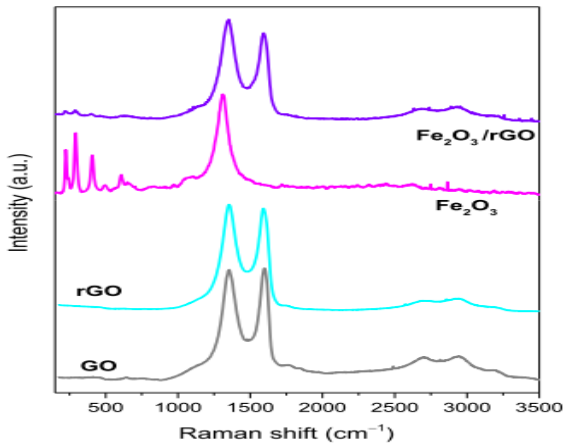

Figure 4. Micro-Raman spectra of the investigated samples

By quantitatively analyzing these spectra, the sample surface composition is estimated, and the resulting weight percent of the oxide in the nanocomposite is evaluated. The relative amounts of carbon, oxygen and iron present on the sample surface are found to be 47.6 at%, 37.5 at% and 14.9 at%, respectively. The relative weight of the α-Fe_2O_3 component in the nanocomposite, calculated on the basis of these results, is 59.3 wt%, slightly higher than that inferred from TGA (52 wt%). Moreover, by subtracting from total oxygen content the contribution present in iron oxide (22.4 at%), oxygen bonded to carbon is found to be 15.2 at%, which gives an oxidation degree of the carbon component of the nanocomposite, as measured by the O/C molar ratio, of 0.32. Comparable results are obtained for bare rGO.

The results of the compositional analysis on GO (C: 63.9 at%; O: 34.9 at%; S: 1.2 at%) reveal that some sulfonic (−SO_3H) acid functionalities are introduced on the sample surface during the oxidative treatment of graphite. By subtracting from total oxygen content the contribution due to sulphonic groups (3.6 at%), oxygen bonded to carbon results to be 31.3 at%, which corresponds to a by far higher oxidation degree (O/C = 0.49). This finding confirms that thermal reduction of GO to rGO occurs during the solvothermal treatment, with 35% decrease of the carbon oxidation degree.

A further incontrovertible evidence of the reduction of GO to rGO emerges from the comparison between the very different HRXPS profiles of the C 1s core levels in GO and Fe_2O_3/rGO nanocomposite (Figure 5a). Both the spectra show the contribution arising from C=C/C−C bonds in aromatic rings at 284.5 eV binding energy (BE). Contributions ascribed to oxygenated carbon species contribute in the 286–290 eV BE range. They include C–O species in phenols and ethers (at 286.1−286.3 eV), C=O species in carbonyls/quinones (at ~287.5 eV), and O–C=O bonds in carboxylic acid and anhydrides and esters (at 288.7−289.3 eV) [22-23, 29].

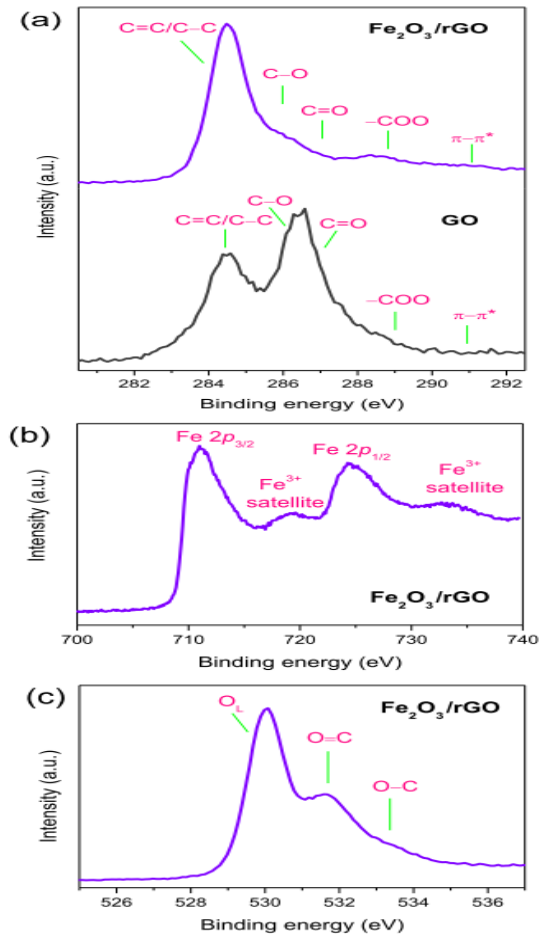

Figure 5. High-resolution photoelectron spectra of the (a) C 1*s*, (b) O 1*s*, and (c) Fe 2*p* core levels in (a−c) Fe_2O_3/rGO nanocomposite and (a) GO

It clearly appears that solvothermal treatment brings about a drastic decrease of the C–O and C=O species present on the carbon surface. In addition, the appearance in the HRXPS spectrum of the nanocomposite of a weak contribution at 290.5−291.0 eV (shake-up π–π* transition [22,29]), absent in the HRXPS spectrum of GO, indicates the partial restoration of the π network following the release of oxygenated functionalities upon thermal treatment.

The HRXPS profile of the Fe 2*p* core level in the bare oxide (not shown for briefness) and in the nanocomposite (Figure 5b) consists of two peaks centered at 711.0 and 724.5 eV BE, and two weaker and broad structures located at about 719 and 732 eV. The two prominent peaks can be assigned to the two spin-orbit components (Fe $2p_{3/2}$ at 719 eV and Fe $2p_{1/2}$ at 732 eV) of Fe^{3+} in α-Fe_2O_3 [30]. The weaker contributions are ascribable to the satellites peculiar to Fe^{3+} ions. Since in iron oxides containing reduced Fe^{2+} ions the Fe $2p_{3/2}$ spin orbit component and the related satellite structure shift at lower BE, (~709.7 and ~715 eV, respectively) [31], the above findings prove that no reduction occurs on the oxide surface.

Consistently, the contribution arising from lattice oxygen (O_L) in α-Fe_2O_3 is detected at 530 eV BE in the HRXPS profile of the O 1*s* core level of the nanocomposite (Figure 5c), together with a weaker, broader and asymmetric contribution peaking at 531.7 eV. Surface-absorbed hydroxyl groups (−OH, at 531.4 eV), as well as residual oxygen species (e.g. C=O, C–O and O–C=O) singly and doubly bound to carbon, contributing to O 1s core level at 533.2 and 531.6 eV, respectively [29].

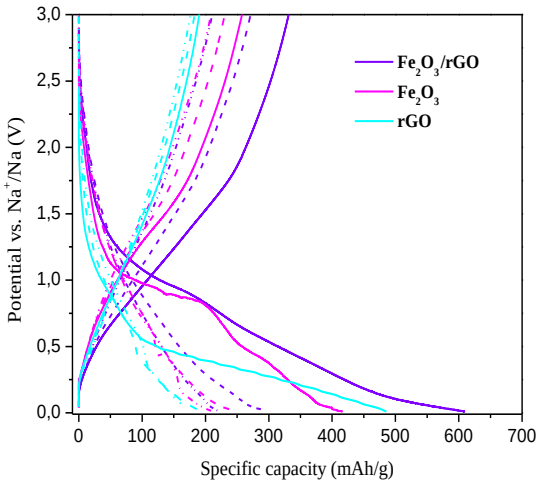

Figure 6. GDC curve of the 1st, 2nd and 5th cycle (continuous, dashed and dash-dotted lines) in the investigated materials

Figure 6 shows the preliminary electrochemical results of five charge/discharge cycles for Fe_2O_3/rGO, bare Fe_2O_3, and rGO. During the first cycle sodiation the nanocomposite shows a capacity of 610 mAh/g, this value is lower compared to the theoretical specific capacity (1007 mAh/g) but higher than the charge obtained from the rGO (415 mAh/g) and the bare Fe_2O_3electrode (485 mAh/g).

Worth to be noted, the nanocomposite and the bare Fe_2O_3 have a similar amount of total carbon content in the electrode so the better performance should be ascribed to the better properties of the nanocomposite, i.e. the presence of the rGO and the intimate connection between the highly conducting graphene sheets and the iron oxide nanoparticles. The same trend is observed in the subsequent de-sodiation and in the following cycles.

As reported in literature, the coulombic efficiency (CE) of the first cycle is quite low: 62.9%, 54.3% and 39.16% for the nanocomposite, the bare Fe_2O_3, and rGO respectively [32]. These low values have been generally attributed to the formation of the solid electrolyte interface (SEI) and irreversible insertion of the sodium into the active material [33]. In all cases, however, the CE rapidly increases during the subsequent cycles, reaching a value higher than 95% after five charge/discharge cycles.

Finally, if we exclude any synergistic effect in the nanocomposite, from the results of the GCPL on the rGO electrode is possible to determine the specific capacity in percentage deriving from the presence of the rGO. This value is found to be between 20 and 30% of the specific capacity resulting from the nanocomposite (22.3% in the first cycle).

4. CONCLUSIONS

In this work, hematite/reduced graphene oxide (Fe_2O_3/rGO) nanocomposite, successfully synthesized via a solvothermal process, has been characterized by means of a combination of complementary techniques and evaluated as anode material in Na-ion rechargeable batteries.

The solvothermal process allows the thermal reduction of GO without the addition of a reducing agent. The α-Fe_2O_3 nanoparticles are uniformly anchored onto the surface of graphene nanosheets and the electronic conductivity of the nanocomposite benefits from such an intimate contact. As a result, the α-Fe_2O_3/rGO-based anode exhibits higher specific capacities compared with that based on the bare α-Fe_2O_3.

Further electrochemical tests are currently in progress in order to evaluate the stability and the rate capability of the α-Fe_2O_3/rGO-based anode.

REFERENCES

[1] Yang Z, Zhang J, Kintner-Meyer MCW, Lu X, Choi D, Lemmon JP, Liu J. (2011). Electrochemical energy storage for green grid. Chem. Rev. 111(5): 3577–3613. http://dx.doi.org/10.1021/cr100290v

[2] Gagliano A, Nocera F. (2017). Analysis of the performances of electric energy storage in residential applications. International Journal of Heat and Technology 35(S1): S41-S48. https://doi.org/10.18280/ijht.35Sp0106

[3] Marom R, Amalraj SF, Leifer N, Jacob D, Aurbach D. (2011). A review of advanced and practical lithium battery materials. J. Mater. Chem. 21(27): 9938-9954. http://dx.doi.org/10.1039/c0jm04225k

[4] Goodenough JB, Park K-S. (2013). The Li-Ion rechargeable battery: A Perspective. J. Am. Chem. Soc. 135(4): 1167–1176. http://dx.doi.org/10.1021/ja3091438

[5] Scrosati B, Hassounab J, Sun YK. (2011). Lithium-ion batteries. A look into the future. Energy Environ. Sci. 4(9): 3287-3295. http://dx.doi.org/10.1039/ c1ee01388b

[6] Slater MD, Kim D, Lee E, Johnson CS (2013). Sodium-ion batteries. Adv. Funct. Mater. 23(8): 947–958. http://dx.doi.org/10.1002/adfm.201200691

[7] Kundu D, Talaie E, Duffort V, Nazar LF. (2015). The emerging chemistry of sodium ion batteries for electrochemical energy storage. Angew. Chem. Int. Ed. 54(11): 3431-3448. http://dx.doi.org/10.1002/anie.201410376

[8] Wang Y, Chen R, Chen T, Lv H, Zhu G, Ma L, Wang C, Jin Z, Liu J. (2016). Emerging non-lithium ion batteries. Energy Storage Mater. 4: 103–129. http://dx.doi.org/10.1016/j.ensm.2016.04.001

[9] Peters J, Buchholz D, Passerini S, Weil M. (2016). Life cycle assessment of sodium-ion batteries. En. Environ. Sci. 9(5): 1744-1751. http://dx.doi.org/10.1039/C6EE00640J

[10] Jian Z, Zhao B, Liu P, Li F, Zheng M, Chen M, Shi Y, Zhou H. (2014). Fe_2O_3 nanocrystals anchored onto graphene nanosheets as the anode material for low-cost sodium-ion batteries. Chem. Commun. 50(10): 1215-1217. http://dx.doi.org/10.1039/C3CC47977C

[11] Fu Y, Wei Q, Wang X, Zhang G, Shu H, Yang X, Tavares AC, Sun S. (2016). A facile synthesis of Fe_3O_4 nanoparticles/graphene for high performance

lithium/sodium-ion batteries. RSC Adv. 6(20): 16624-16633. http://dx.doi.org/10.1039/C5RA25835A

[12] Li F, Jiang X, Zhao J, Zhang S. (2015). Graphene oxide: A promising nanomaterial for energy and environmental applications. Nano Energy 16: 488-515. https://doi.org/10.1016/j.nanoen.2015.07.014

[13] Zhu J, Zhu T, Zhou X, Zhang Y, Lou XW, Chen X, Zhang H, Hng HH, Yan Q. (2011). Facile synthesis of metal oxide/reduced graphene oxide hybrids with high lithium storage capacity and stable cyclability. Nanoscale 3(3): 1084-1089. http://dx.doi.org/10.1039/C0NR00744G

[14] Zhang ZJ, Wang YX, Chou SL, Li HJ, Liu HK, Wang JZ. (2015). Rapid synthesis of α -Fe_2O_3/rGO nanocomposites by microwave autoclave as superior anodes for sodium-ion batteries. J. Power Sources 280: 107-113. https://doi.org/10.1016/j.jpowsour.2015.01.092

[15] Hummers Jr. WS, Offeman RE. (1958). Preparation of Graphitic Oxide. J. Am. Chem. Soc. 80(6): 1339-1339. http://dx.doi.org/10.1021/ja01539a017

[16] Alcántara R, Jiménez-Mateos JM, Lavela P, Tirado JL. (2001). Carbon black: a promising electrode material for sodium-ion batteries. Electrochem. Commun. 3(11): 639-642. http://dx.doi.org/10.1016/S1388-2481(01)00244-2

[17] Fathy M, Gomaa A, Taher FA. El-Fass MM, Kashyout AEl-HB. (2016). Optimizing the preparation parameters of GO and rGO for large-scale production. J. Mater. Sci. 51(12): 5664–5675. http://dx.doi.org/10.1007/s10853-016-9869-8

[18] Wang HW, Hu ZA, Chang YQ, Chen YL, Zhang ZY, Yang YY, Wu HY. (2011). Preparation of reduced graphene oxide/cobalt oxide composites and their enhanced capacitive behaviors by homogeneous incorporation of reduced graphene oxide sheets in cobalt oxide matrix. Mater. Chem. Phys. 130(1-2): 672–679. https://doi.org/10.1016/j.matchemphys. 2011.07.043

[19] Wang YX, Chou SL, Liu HK, Dou SX. (2013). Reduced graphene oxide with superior cycling stability and rate capability for sodium storage. Carbon 57: 202-208. http://dx.doi.org/10.1016/j.carbon.2013.01. 064

[20] Liu X, Chen T, Chu H, Niu L, Sun Z, Pan L, Sun CQ. (2015). Fe_2O_3-reduced graphene oxide composites synthesized via microwave-assisted method for sodium ion batteries. Electrochim. Acta 166(1): 12-16. https://doi.org/10.1016/j.electacta.2015.03.081

[21] Ferrari AC, Robertson J. (2001). Interpretation of Raman spectra of disordered and amorphous carbon, Phys. Rev. B 61(20): 14095–14107. http://dx.doi.org/10.1103/PhysRevB.61.14095

[22] Santangelo S. (2016). Controlled surface functionalisation of carbon nanotubes by nitric acid vapors generated from sub-azeotropic solution. Surf. Interf. Analysis 48(1): 17–25. https://doi.org/10.1002/sia.5875

[23] Zhang R, Santangelo S, Fazio E, Neri F, D'Arienzo M, Morazzoni F, Zhang Y, Pinna N, Russo PA. (2015). Stabilization of TiO_2 nanoparticles at the surface of carbon nanomaterials promoted by microwave heating. Chemistry – A European Journal 21(42): 14901–14910. https://doi.org/10.1002/chem. 201502433

[24] Chernyshova IV, Hochella Jr M., Madden AS. (2007). Size-dependent structural transformations of hematite nanoparticles. 1. Phase transition. Phys. Chem. Chem. Phys. 9(14): 1736–1750. http://dx.doi.org/10.1039/B618790K

[25] Chaudhari S, Srinivasan M. (2012). 1D hollow α-Fe_2O_3 electrospun nanofibers as high performance anode material for lithium ion batteries. J. Mater. Chem. 22(43): 23049–23056. http://dx.doi.org/10.1039/C2JM32989A

[26] Cesar I, Sivula K, Kay A, Zboril R, Grätzel M. (2009). Influence of feature size, film thickness, and silicon doping on the performance of nanostructured hematite photoanodes for solar water splitting. J. Phys. Chem. C 113(2): 772–782. http://dx.doi.org/ 10.1021/jp809060p

[27] Santangelo S, Frontera P, Pantò F, Stelitano S, Marelli M, Malara F, Patané S, Dal Santo V, Antonucci PL. (2017). Effect of Ti- or Si-doping on nanostructure and photo-electro-chemical activity of electro-spun iron oxide fibres. Int. J. Hydrogen En. 42(46): 28070-28081. http://dx.doi.org/10.1016/j.ijhydene.2017.03. 204

[28] Bersani D, Lottici PP, Montenero A. (1999). Micro-Raman Investigation of Iron Oxide Films and Powders Produced by Sol–Gel Syntheses. J. Raman Spectrosc. 30(5): 355–360. https://doi.org/10.1002/(SICI)1097-4555(199905)30:5<355:AID-JRS398>3.0.CO;2-C

[29] Santangelo S, Piperopoulos E, Fazio E, Faggio G, Ansari S, Lanza M, Neri F, Messina G, Milone C. (2014). A safer and flexible method for the oxygen functionalisation of carbon nanotubes by nitric acid vapors. Appl. Surf. Sci. 303: 446–455. https://doi.org/10.1016/j.apsusc.2014.03.023

[30] Baltrusaitis J, Cwiertny DM, Grassian VH. (2007). Adsorption of sulfur dioxide on hematite and goethite particle surfaces. Phys. Chem. Chem. Phys. 9(41): 5542–5554. http://dx.doi.org/10.1039/b709167b

[31] Saremi-Yarahmadi S, Wijayantha KGU, Tahir AA, Vaidhyanathan B. (2009). Nanostructured α-Fe_2O_3 electrodes for solar driven water splitting: effect of doping agents on preparation and performance. J. Phys. Chem. C 113(12): 4768–4778. http://dx.doi.org/10.1021/jp808453z

[32] Klein F, Jache B, Bhide A, Adelhelm P. (2013). Conversion reactions for sodium-ion batteries. Phys. Chem. Chem. Phys. 15(38): 15876-15887. http://dx.doi.org/10.1039/c3cp52125g

[33] Fiore M, Longoni G, Santangelo S, Pantò F, Stelitano S, Frontera P, Antonucci PL, Ruffo R. (2018). Electrochemical characterization of highly abundant, low cost iron (III) oxide as anode material for sodium-ion rechargeable batteries. Elettrochim. Acta 269: 367-377. http://dx.doi.org/10.1016/j.electacta.2018.02.161